CrystEngComm

PAPER

View Article Online
View Journal | View Issue

Cite this: *CrystEngComm*, 2021, **23**, 4954

Photodiodes based on a $MAPbBr_3/Bi^{3+}$-doped $MAPbCl_3$ single crystals heterojunction for the X-ray detection†

Yuzhu Pan,[a] Xin Wang,*[a] Jingda Zhao,[a] Yubing Xu,[a] Yuwei Li,[a] Qing Li,[a] Xiaobing Zhang,[a] Zhiwei Zhao,[a] Zhuoya Zhu,[a] Chen Jing,[a] Wu Jun,[a] Elias Emeka Elemike,[b] Byung Seong Bae[c] and Wei Lei*[a]

Received 26th March 2021,
Accepted 13th June 2021

DOI: 10.1039/d1ce00406a

rsc.li/crystengcomm

Perovskite single crystals (PSCs) can be used to fabricate high performance photoelectric detectors due to their superior optoelectronic characteristics. Generally, an external electric field needs to be applied in PSC-based detectors to improve their charge collection efficiency. However, the large external electric field increases the dark current, which will enlarge the noise current. To alleviate this drawback, an approach of fabricating a PSC-based heterojunction is proposed in this work, which contributes to reduced dark current in a relatively high reverse electric field. In this study, a heterojunction formed by epitaxially growing $MAPbBr_3$ PSCs on Bi^{3+}-doped $MAPbCl_3$ PSCs is reported, and it shows relatively low trap density and higher built-in potential. The as-fabricated Au-$MAPbBr_3/Bi^{3+}$-doped $MAPbCl_3$ PSC heterojunction-Au photodiode shows smaller dark current density, better long-term current stability and reduced noise level by approximately four orders compared to the Au–$MAPbBr_3$ PSCs–Au photoconductor device under an external reverse voltage of 100 V (mean electric field of ~31.5 V mm^{-1}). Moreover, the pN heterojunction photodiode shows favorable X-ray detection performance, with a fast response time of 4.89 μs and high sensitivity of 1.72×10^3 μC Gy_{air}^{-1} cm^{-2} for 50 kVp X-ray photons under a reverse electric field of 31.5 V mm^{-1}. This work confirms that the epitaxial fabrication of PSC heterojunctions may be a promising strategy to enhance the performance of X-ray photodetectors.

Introduction

Organic–inorganic halide perovskites ($MAPbX_3$, where MA = CH_3NH_3, X = Cl, Br, I) have received a tremendous amount of attention in recent decades due to their intriguing optical and electronic properties,[1–3] which have been employed in a number of optoelectronic devices, including photodetectors,[4,5] light-emitting diodes,[6,7] lasers[8,9] and solar cells.[10–12] In comparison with polycrystalline thin films, perovskite single crystals (PSCs) are free of grain boundaries and exhibit lower charge trap densities, higher mobility–lifetime products, and better stability.[13–16] In addition, due to their high-Z elements (Pb, Br, I, *etc.*) and thicknesses of a few millimeters, single crystal bulk perovskites have been successfully utilized as active absorbers with high attenuation coefficients for direct X-ray photon to current conversion.[17–19] Most reported frameworks of direct X-ray detectors based on PSCs are perovskite crystals sandwiched between two metal electrodes. In these frameworks, charges generated by incident X-ray photons are shifted in PSCs and collected by electrons on both sides of the crystal under the external electric field. Generally, the applied external electric field is expected to be high to increase the drift length of charge carriers and reduce the charge trapping; however, this will also decrease the signal-noise ratio due to the increase of dark current.[20] To improve the charge collection while decreasing the dark current at a high electric field, several approaches have been presented to overcome this drawback, including growing high quality alloyed perovskite SCs to improve bulk resistivity and using a guard ring electrode in the detector to reduce the crystal surface leakage current,[21] forming a Schottky contact barrier by depositing an asymmetrical electrode on a crystal surface to reduce the dark current of the device,[22,23] introducing an electron transport layer and hole transport layer to block injected electrons and holes,[24,25] and selecting an exposed facet with improved charge carrier transport properties and a lower trap density.[26]

---

[a] *School of Electronic Science and Engineering, Joint International Research Laboratory of Information Display and Visualization, Southeast University, Nanjing, China. E-mail: 230159424@seu.edu.cn, lw@seu.edu.cn*
[b] *Chemistry Department of North West University, South Africa*
[c] *Department of Electronics & Display Engineering, Hoseo University, Hoseo Ro 79, Asan City, Chungnam 31499, Korea*

† Electronic supplementary information (ESI) available. See DOI: 10.1039/d1ce00406a

In spite of this progress, little work has been carried out to study X-ray pN junction photodiodes based on PSCs, which is an efficient stratagem to reduce dark current even at a high reverse voltage. In our previous work, we reported the fabrication of heterojunctions by epitaxially growing $MAPbBr_xCl_{3-x}$ on $MAPbCl_3$ PSCs and their successful application in X-ray detection.[27–29] To further decrease the dark current of a heterojunction photodiode, it is significant to enlarge the heterojunction barrier.

Similar to silicon, gallium nitride, indium phosphide and other conventional semiconductors, the incorporation of impurity ions into perovskites can tune their optical and electrical properties and realize controlled incorporation of n-type or p-type dopants.[30] Recently, a report of the successful addition of isovalent and heterovalent ions to perovskite was published.[31,32] Especially for the PSCs with Bi^{3+} incorporation, positive effects were observed, such as prolonged stability, enhancement in the n-type electrical conductivity and red shifts of the absorption onset energy.[33–36] However, subsequent studies have also reported that the addition of Bi^{3+} to perovskite crystal increases the within-gap trap states.[34,37–39] This defect causes higher dark current and deterioration of optoelectronic properties, and photoelectric devices directly based on Bi-doped perovskite materials have been rarely reported to date.

Inspired by the above work, we herein report a structure of a pN photodiode based on an $MAPbBr_3/Bi^{3+}$-doped $MAPbCl_3$ PSC heterojunction. $MAPbBr_3$ PSCs have already been proved to be slightly p-type semiconductors.[21,28] Bi^{3+} ions doped into $MAPbCl_3$ PSCs with a larger band gap could enhance their n-type conductivity, as with the incorporation of Bi^{3+} in $MAPbBr_3$ and $CsPbBr_3$.[32,40] The large barrier in the heterojunction could suppress the dark current effectively. In this work, Bi^{3+}-doped $MAPbCl_3$ PSCs were dipped into $MAPbBr_3$ precursor solution with several hours of epitaxial growth to fabricate pN heterojunctions. Considering the similar lattice constants of Bi^{3+}-doped $MAPbCl_3$ and $MAPbBr_3$ PSCs, this could support the fabrication of photodiodes based on a pN type PSC heterojunction with a small lattice mismatch rate (~1.65%) and lower carrier trap density at the interface. The as-fabricated pN photodiodes based on the $MAPbBr_3/Bi^{3+}$-doped $MAPbCl_3$ PSC heterojunction exhibit rectification characteristics and maintain a small dark current density when a large reverse bias is applied (>100 V). Compared to the Au–$MAPbBr_3$–Au photoconductor device, the pN PSC heterojunction photodiode shows smaller dark current density, improved long term current stability and a lower noise level under the same conditions due to the built-in space charge region. In addition, under a reverse bias of 100 V, the pN PSC heterojunction photodiode in this work suggests a fast response time of 4.89 μs and good X-ray detection performance, with a sensitivity of 1.72×10^3 μC Gy_{air}^{-1} cm^{-2} for 50 kVp X-ray photons. This work reports a photoelectric device utilizing Bi^{3+}-doped $MAPbCl_3$ PSCs and proposes an ideal method to obtain building blocks for sensitive X-ray photodetectors.

Experimental section

Material preparation

Methylamine ethanol solution (CH_3NH_2, 33 wt%), hydrobromic acid (HBr, 48 wt%), and hydrochloric acid (HCl, 37 wt%) were obtained from Aladdin. *N*,*N*-Dimethylformamide (DMF) and dimethyl sulfoxide (DMSO) were obtained from Alfa Aesar. Lead chloride ($PbCl_2$, 99.9%), lead bromide ($PbBr_2$, 99.9%) and bismuth(III) chloride ($BiCl_3$, ≥98%) were purchased from Sigma-Aldrich. All commercial products were used as received.

Heterojunction device fabrication:

To synthesize methylamine chloride (MACl) and methylamine bromide (MABr), 1 mol L^{-1} HCl and 1 mol L^{-1} HBr were poured into 1 mol L^{-1} CH_3NH_2 solution, respectively. To increase the purity of the MACl and MABr powder, the raw powder was washed with ethanol and diethyl ether at least three times. White powder-like MACl and MABr were obtained after drying in vacuum at 150 °C. The optimized inverse temperature crystallization (ITC) method was used to grow halide perovskite crystals in this work according to previously published work.[36,41–43] The Bi^{3+}-doped $MAPbCl_3$ PSCs could be grown by dissolving MACl (2.025 g), $PbCl_2$ (8.34 g) and $BiCl_3$ (0.946 g) in a 1 : 1 : 0.1 molar ratio in mixed solution with 30 mL DMF and 20 mL DMSO. To prepare the precursor solutions of $MAPbBr_3$, MABr (3.36 g) and $PbBr_2$ (11.01 g) in a 1 : 1 molar ratio was dissolved in 30 mL DMF. For the synthesis of the wrapped perovskite pN heterojunction, 10% Bi^{3+}-doped $MAPbCl_3$ precursor solution was firstly heated from 40 °C to 60 °C over several days to obtain n-type PSCs. Then, the obtained n-type PSCs were placed into the $MAPbBr_3$ precursor solution and epitaxially grown for several hours at 60 °C. Finally, the core-shell wrapped $MAPbBr_3/Bi^{3+}$-doped $MAPbCl_3$ PSC heterojunction bulks were obtained. The surrounding redundant parts of the as-fabricated core–shell wrapped heterojunction bulks were cut away using a fine diamond-impregnated wire sawing machine. To fabricate the heterojunction photodiodes with vertical structures, two Au (50 nm) electrodes were deposited on the two opposite surfaces of the heterojunction bulk by thermal evaporation in vacuum, respectively. The as-presented device in this work had an efficient electrode area of 16 mm^2 and thickness of 3.18 mm. For comparison, an Au–$MAPbBr_3$–Au device with an efficient electrode area of 25 mm^2 and thickness of 2.91 mm was fabricated using the same approaches.

Device characterization and measurements:

SEM (scanning electron micrograph) images were obtained by a Quanta 200 FEI microscope (USA). PL (photoluminescence) patterns were obtained by an Edinburgh Instruments FS5 (UK) using a 355 nm pulsed Nd:YAG laser as the excitation source. Current–voltage (*I*–*V*) characteristics were measured by a Keithley 4200 semiconductor analyzer (USA) under room temperature. The responsivity spectra were measured using a Zolix tunable 500 W xenon arc lamp light as the illumination source and a Keithley 4200 semiconductor analyzer. The response time was measured using an Agilent oscilloscope (7.5G, USA) with a Keithley 2400 voltage source (USA) and a 532 nm pulsed Nd:YAG laser with a 6 ns pulse width at 20 Hz as the illumination source. The photocurrent in the X-ray detection performance was measured by a Keithley 6487 picoammeter. The 50 kVp X-ray photons were obtained from a digital radiography (DR) system with a setting tube voltage of 50 kV, which was provided by Perlove Medical (China). The dependence of the X-ray dose rate on the operating current of the X-ray tube was determined by a commercial dosimeter (FJ-347A, China).

Results and discussion

A detailed schematic of the perovskite pN heterojunction fabrication process is illustrated in Fig. 1. The Bi^{3+}-doped $MAPbCl_3$ precursor solution was decanted into a crystalline dish, and then the n-type Bi^{3+}doped $MAPbCl_3$ PSCs were grown from 40 °C to 60 °C. Subsequently, the as-fabricated n-type Bi^{3+}-doped $MAPbCl_3$ PSCs were placed into an intrinsic $MAPbBr_3$ precursor solution at 60 °C, and then p-type $MAPbBr_3$ PSCs were epitaxially grown on the n-type Bi^{3+}-doped $MAPbCl_3$ PSCs to form a wrapped external layer. After cutting the redundant parts around the crystal bulk, a perovskite pN heterojunction with a thickness of 3.18 mm was fabricated in which the thicknesses of Bi^{3+}-doped $MAPbCl_3$ (yellow) and $MAPbBr_3$ (orange) were 1.68 mm and 1.50 mm, respectively.

The digital photograph of the as-fabricated PSC heterojunction is shown in the inset of Fig. 2(a), from which a clear interface can be easily observed. More details of the as-fabricated heterojunction interface could be obtained from the cross-sectional scanning electron micrograph (SEM) image, which reveals the favorable contact between the $MAPbBr_3$ and Bi^{3+}-doped $MAPbCl_3$ PSCs. This finding is attributed to the similar lattice constants of Bi^{3+}-doped $MAPbCl_3$ (~5.6815 Å) and $MAPbBr_3$ PSCs (~5.8715 Å), with a lattice mismatch rate of approximately 1.65%, as shown in Fig. 2(b). The measured Bi/Pb atomic ratio (~0.076) of the Bi-doped $MAPbCl_3$ crystals, identified using energy dispersive X-ray spectroscopy (EDS), was found to be substantially lower than the nominal Bi/Pb amount (0.1) in the precursor solution, as shown in the ESI† (Fig. S1). This indicates the formation of Pb vacancies and the superior difficulty of doping perovskites.[32,34] Furthermore, the steady-state photoluminescence (PL) of $MAPbCl_3$, Bi^{3+}-doped $MAPbCl_3$ and the $MAPbBr_3$ PSC heterojunction was investigated with a 355 nm pulsed laser as the excitation light source. As shown in Fig. 2(c), we observed a large decrease in the PL spectral intensity for $MAPbCl_3$ after Bi^{3+} incorporation. This degradation in PL intensity should be ascribed to increased non-radiative recombination in Bi-doped $MAPbCl_3$, which is consistent with the previous results for Bi-doped $MAPbBr_3$ and $CsPbBr_3$.[37,40]

To fabricate the photodiode, the as-fabricated $MAPbBr_3$/Bi^{3+}-doped $MAPbCl_3$ PSC heterojunction was sandwiched by two Au electrodes deposited by thermal evaporation. The $MAPbBr_3$/Bi^{3+}-doped $MAPbCl_3$ PSC heterojunction bulk is the active layer for generating and transporting carriers. The Au electrodes on the Bi^{3+}-doped $MAPbCl_3$ and $MAPbBr_3$ surfaces are the anode and cathode, respectively. To shed light on the operation mechanism of the heterojunction photodiode, the energy band diagram of the photodiode in the equilibrium state under the reverse bias condition was then analyzed. The detailed energy band positions of the various PSCs are shown in the ESI† (Fig. S2) according to results reported previously.[28,32,34,36,42] As clearly depicted in Fig. 3(a), the $MAPbBr_3$/Bi^{3+}-doped $MAPbCl_3$ PSC heterojunction shows a typical type II (staggered) energy band structure. After the p-type $MAPbBr_3$ and n-type Bi^{3+}-doped $MAPbCl_3$ contact each other, a built-in electric field pointed from n-type PSCs to p-type PSCs can be formed at the interface due to band

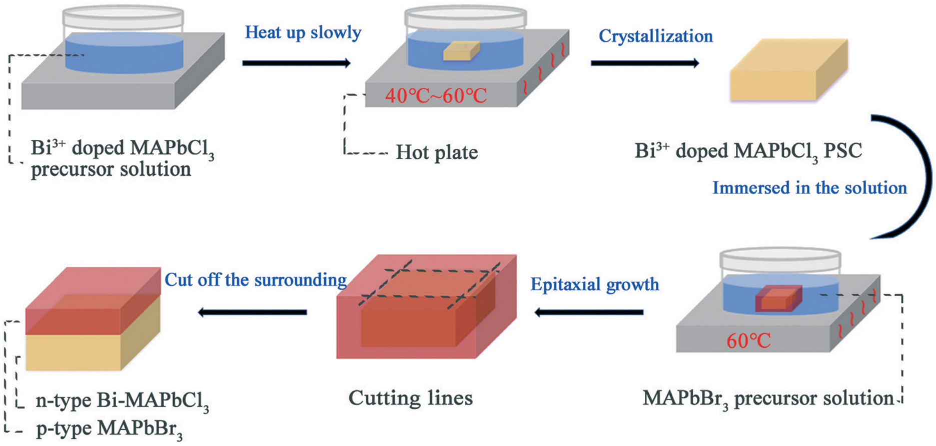

Fig. 1 Schematic of the fabrication of the $MAPbBr_3$/Bi^{3+}-doped $MAPbCl_3$ PSC heterojunction by solution-process epitaxial growth.

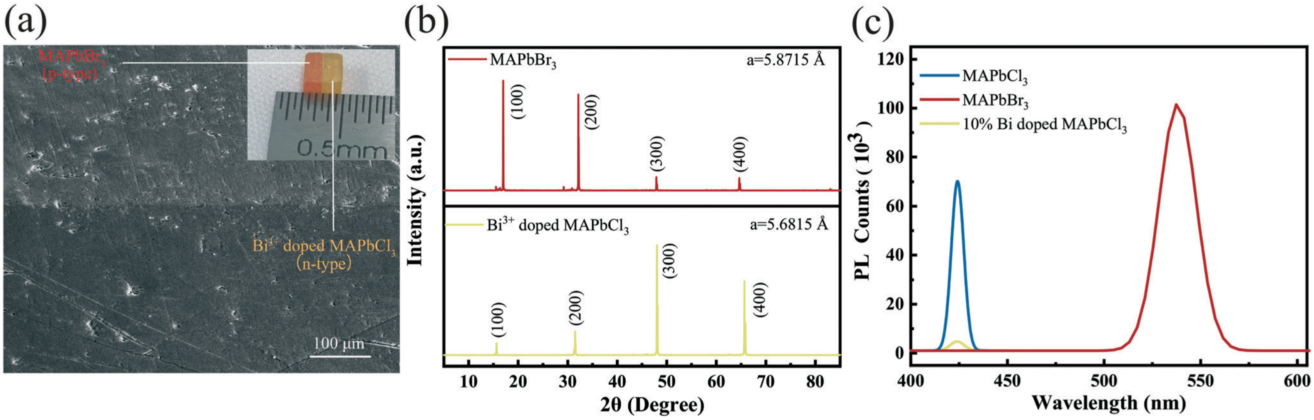

Fig. 2 (a) Cross-sectional SEM images of the as-fabricated pN PSC heterojunction. Inset: A digital photograph of the junction. (b) XRD spectra and (c) normalized PL spectra of two regions of the as-fabricated PSC heterojunction for $MAPbBr_3$ and Bi^{3+}-doped $MAPbCl_3$, respectively.

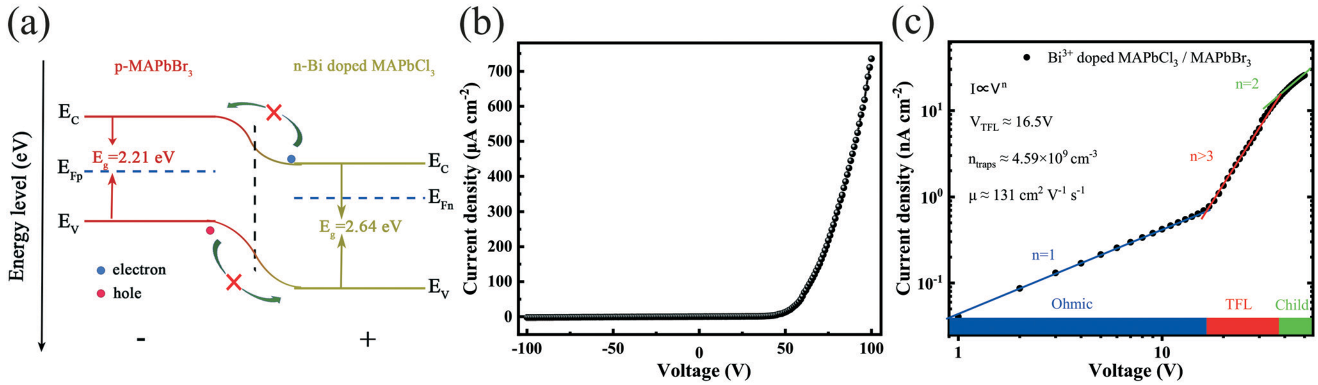

Fig. 3 (a) Energy band diagram of the pN PSC heterojunction photodiode in the equilibrium state under reverse bias conditions. (b) *I–V* curve of the PSC heterojunction pN photodiode with bias sweeping from negative to positive. (c) Dark *I–V* response of the heterojunction device exhibiting different regions obtained from the log *I versus* log *V* plot.

bending. The energy barriers of the VBM (valance band maximum) and CBM (conduction band minimum) between $MAPbBr_3$ and the Bi^{3+}-doped $MAPbCl_3$ PSCs are estimated to be about 0.86 eV and 0.43 eV, respectively. Under a reverse external bias, the increased energy band barrier of the PSC heterojunction would effectively prevent electrons and holes from traversing the space charge region, which contributes to decreasing the dark current. As can be observed in Fig. 3(b), the *I–V* curve of the pN heterojunction photodiode shows typical rectification characteristics, which reveals a very small dark current under reverse bias sweep.

The conventional space charge limited current (SCLC) method is employed to investigate the transport properties of a device. The trap density (n_{trap}) and carrier mobility (μ) of the device can be derived from measuring the dark *I–V* curve. The dark *I–V* curve can be divided three regions, which are the linear ohmic region (blue), trap-filled region (red), and trap-free child region (green), as shown in Fig. 3(c). The linear *I–V* relation in the dark (blue line) indicates an ohmic response at low bias. Through the trap filling limited (TFL) region, the trap density was calculated based on the following equation:[2]

$$n_{\mathrm{trap}} = \frac{2V_{\mathrm{TFL}}\varepsilon\varepsilon_0}{eL^2} \tag{1}$$

where e, ε_0, ε and L are the electronic charge, vacuum permittivity, relative dielectric constant and thickness of the device, respectively. V_{TFL} is the voltage of the trap filling limit.

When operating in the trap-free child region, the carrier mobility (μ) of the device was fitted by the Mott–Gurney law:[44]

$$\mu = \frac{8JL^3}{9\varepsilon\varepsilon_0 V^2} \tag{2}$$

where V and J represent the applied voltage and dark current density in the child region, respectively.

Depending on the V_{TFL} (~16.5 V) and ε (~25) for the $MAPbBr_3$/Bi^{3+}-doped $MAPbCl_3$ PSC heterojunction, the trap density and mobility of the heterojunction were estimated to be about 4.59×10^9 cm^{-3} and 131 cm^2 V^{-1} s^{-1}, respectively, suggesting fantastic charge transport and collection efficiency.

Assuming a uniform electric field inside device, the single polarity Hecht equation could be adapted as:[45]

$$\eta = \frac{Q}{Q_0} = \mu\tau\frac{U}{d^2}\left(1 - e^{-d^2/\mu\tau U}\right) \tag{3}$$

where η is the charge collection efficiency (CCE), U is the applied voltage, d is the detector thickness, and $\mu\tau$ is the mobility and transit time product. According to the above equation, it is clear that the applied electric field in the device is required to be higher to increase the charge collection efficiency. However, the dark current would be enlarged at the same time that the applied voltage increases, which would decrease the signal-to-noise ratio and degrade the detection performance of the device. It is significant for photoelectrical detectors to maintain a small dark current at a relatively high applied external voltage. According to the literature,[46,47] simulation of perovskite p–n heterojunctions was performed by multiphysics analysis in COMSOL, as shown in the ESI,† to investigate the mechanism and advantages. The simulation model is shown in Fig. S6.† The energy diagrams for the perovskite homo-junction and hetero-junction are compared in Fig. S7,† which indicates that the hetero-junction can further efficiently suppress the diffusion of holes from the p-type region due to the larger energy barrier of the valance band in the heterojunction. The simulation results also show that the dark current of the perovskite pN junction is quite small although a high reversed bias voltage is applied (Fig. S8†), and the nonequilibrium photo-current density is quite stable (Fig. S9†). For the heterojunction with a large bandgap in the n-type region, the dark current could be suppressed effectively, especially for the high bias electric field, as shown in Fig. S10.† The simulation proves that the perovskite heterojunction based on n-type large bandgap perovskite Bi^{3+}-doped $MAPbCl_3$ is significant to further decrease the dark current.

As shown in Fig. 4(a), the dark current of the present heterojunction photodiode is reduced by approximately two orders compared with that of the Au–$MAPbBr_3$–Au photoconductor under the reverse bias voltage. The smaller dark current of the present PSC heterojunction device under reverse bias is attributed to the enlarged barrier of the pN heterojunction, which prevents the electrons and holes from traversing the space charge region. The long-term dark current stability of the two devices at −100 V is also shown in Fig. 4(b). The amplitude of the vibration of the dark current for the PSC heterojunction photodiode is less than 0.78 nA, suggesting better long-term stability under a large reverse external electric field than that of the Au–$MAPbBr_3$–Au photoconductor. Furthermore, the noise spectral density could be analyzed by fast Fourier transform (TTF) of the dark current. The results shown in Fig. 4(c) indicate that the present $MAPbBr_3/Bi^{3+}$-doped $MAPbCl_3$ PSC heterojunction photodiode possesses a relatively low noise level and decreases the noise current by 4 orders compared to the Au–$MAPbBr_3$–Au photoconductor device.

To investigate the photoelectricity properties of the present pN PSC heterojunction device, the J–V curve under light illumination with a 4 mW, 520 nm LED as the light source is measured in Fig. 5(a), and the working mode of the device under reverse bias with incident photons from the anode is illustrated in the inset. The $\mu\tau$ product of the as-fabricated pN PSC heterojunction was extracted by fitting the J–V response with the single-carrier Hecht equation. The $\mu\tau$ product was fitted as about 4.12×10^{-4} cm^2 V^{-1}, indicating a favorable charge collection efficiency for the PSC heterojunction device. The photocurrent density of the heterojunction photodiode approaches the saturation threshold with enlarged external bias and was tested as 302 μA cm^{-2} at −100 V, suggesting relatively high sensitivity. The spectral photoresponse at −100 V was further measured under illumination of a xenon lamp with varied wavelengths. The responsivity (R) could be calculated by the following equation:[48]

$$R = \frac{I_\lambda - I_d}{P_\lambda S} \tag{4}$$

where I_λ is the photocurrent, I_d is the dark current, P_λ is the incident light power intensity, and S is the effective

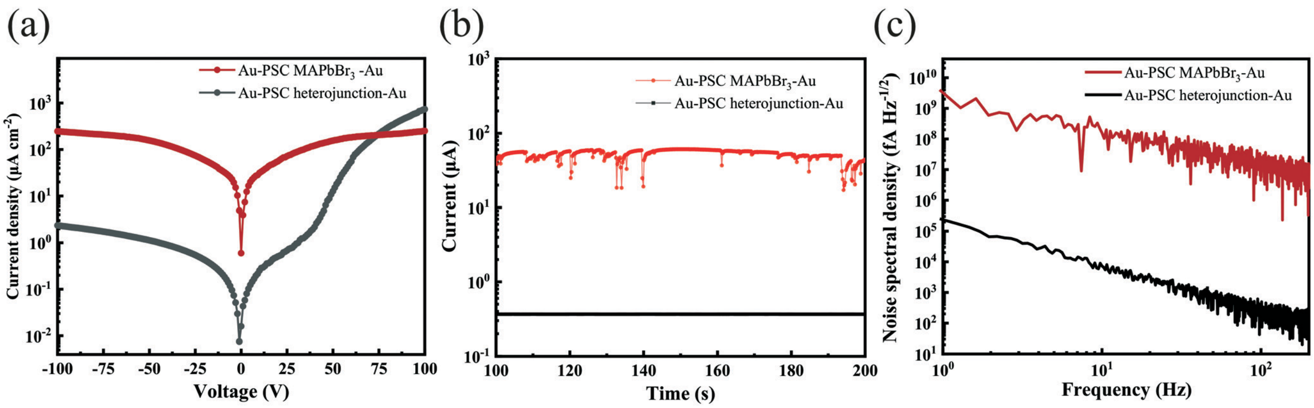

Fig. 4 (a) I–V curves of the PSC heterojunction device and Au–$MAPbBr_3$–Au device in the dark. (b) Long-term dark current stability of the PSC heterojunction device and Au–$MAPbBr_3$–Au device under an external reverse voltage of 100 V. (c) The noise spectral density of the PSC heterojunction device and Au–$MAPbBr_3$–Au device based on the Fourier transform of the dark current.

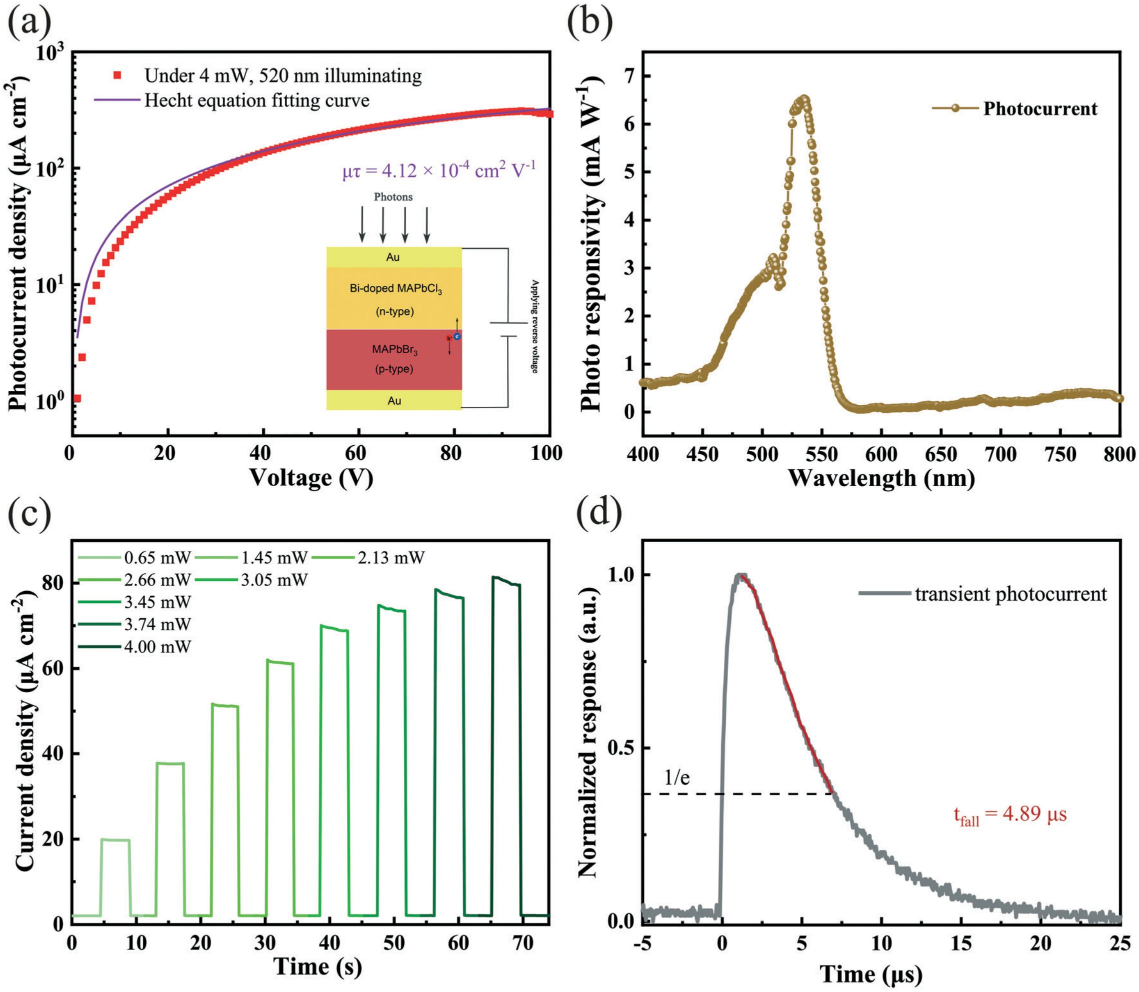

Fig. 5 (a) Photocurrent of the PSC heterojunction device illuminated under a 4 mW, 520 nm LED with increasing applied voltage. Inset: Device structure and working mechanism of the pN PSC heterojunction photodiode as the photodetector and X-ray detector. (b) The spectral response of the PSC heterojunction photodetector. (c) Long term on–off photocurrent of the PSC heterojunction device at −50 V under 520 nm light illumination with different light intensities. (d) Normalized transient current response of the PSC heterojunction device.

illuminated area. From the spectral photoresponse shown in Fig. 5(b), the present pN heterojunction device exhibits a relatively narrow bandwidth response with a peak at 540 nm. The peak corresponds to the reported absorption peak of the $MAPbBr_3$ PSCs.[41] It is worth noting that the responsivity of the device before 450 nm is much lower, although the absorption edge of the Bi^{3+}-doped $MAPbCl_3$ PSCs could be 480 nm (Fig. S3†).[36] This probably occurs because of the presence of the DX-like center (D: donor atom, X: unspecified lattice defect), a nonradiative recombination center, in Bi-doped halide perovskites. It has been hypothesized that electrons are trapped in the DX-like centers and recombine with holes from the valence band, leading to the fast decay of photocurrent, as proposed by Md Azimul Haque *et al.*[35] The current–voltage curves (Fig. S4†) and transient photocurrent (Fig. S5†) of the doped $MAPbCl_3$ were also measured under white light on–off switching, and the results are consistent with the results for doped $MAPbBr_3$.[35] Furthermore, the on–off switching properties of the $MAPbBr_3$/Bi^{3+}-doped $MAPbCl_3$ PSC heterojunction photodiode are presented in Fig. 5(c). It is obvious that the device can be switched on and off repeatedly and stably with different irradiance power densities illuminated by a 420 nm LED. To further investigate the response speed of the heterojunction photodiode, the transient photoresponse signal was measured using a pulsed Nd:YAG laser with a 6 ns pulse width at 20 Hz and recorded by an oscilloscope. The photodetectors collect the pulsed light signal emitted by a pulsed laser, and then the photogenerated carriers can be driven by a built-in potential field or external voltage bias applied to the respective electrodes. Therefore, the response speed can be defined as the photocurrent decay time from the peak down to approximately 1/e. As shown in Fig. 5(d), the device shows a fast response speed with a fall time (t_{fall}) of 4.89 μs in an electric field of 31.5 V mm^{-1}.

It is noted that the as-fabricated $MAPbBr_3$/Bi^{3+}-doped $MAPbCl_3$ PSC heterojunction photodiodes have great potential in direct X-ray detection due to their thicknesses of

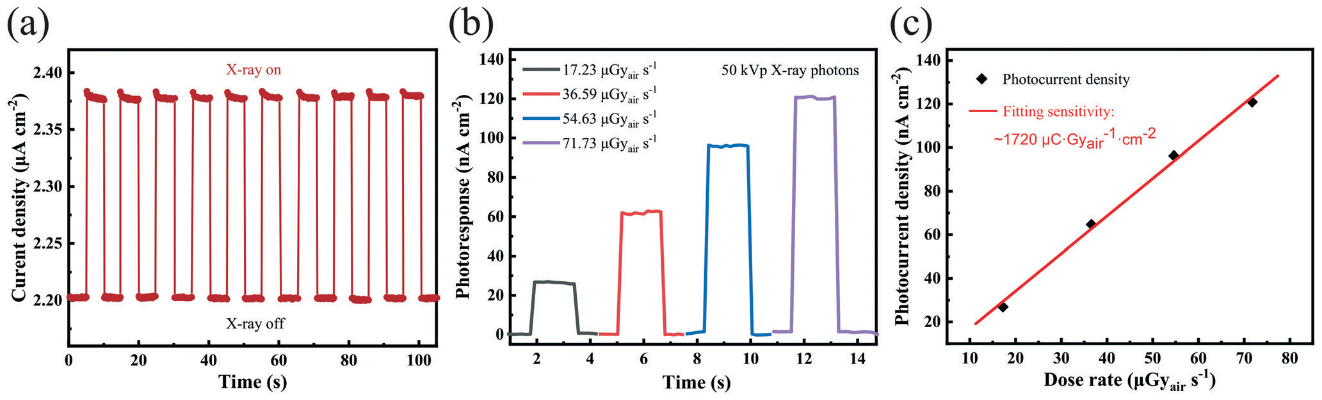

Fig. 6 (a) Current on and off responses of the PSC heterojunction device under a 50 kV, 4 mA X-ray tube. (b) Photocurrent of the PSC heterojunction device at −100 V under irradiation of 50 kVp X-rays with different dose rates. (c) Photocurrent density of the PSC heterojunction devices under different X-ray dose rates, with the sensitivity derived by fitting the slope.

Table 1 Summary of the X-ray detection performance of organic/inorganic lead bromide PSCs-based X-ray detectors.

Devices	X-ray source (keV/kVp)	Sensitivity (μC Gy$_{air}$$^{-1}$ cm^{-2})	Response/decay time (μs)	Reference
Au/MAPbBr$_3$ SC/Au	50 keV	62	272 ± 5	23
Al/MAPbBr$_3$ SC/Au	50 keV	359	76.2 ± 2.5	23
Au/CsPbBr$_3$/Au	80 kVp	61	NA	50
Al/CsPbBr3/Au	80 kVp	1256	NA	50
Au/MAPbBr$_3$ SC/C$_{60}$/BCP/Ag or Au	50 kVp	80	216	51
AZO/MAPbBr$_3$ SC/Au	80 kVp	529	NA	52
Au/poly-TPD/MAPbBr$_{2.5}$Cl$_{0.5}$ PSCs/MAPbCl$_3$ PSCs/Ag	40 kVp	7080	10	27
Au/MAPbBr$_3$/Bi^{3+} doped MAPbCl$_3$ SC/Au	50 kVp	1720	4.89	This work

several millimeters and small dark currents under a large reverse external voltage. The on–off current response of the heterojunction device under 50 kVp X-rays was also measured at −100 V, as shown in Fig. 6(a), which means that it is highly reproducible and stable in air. The photocurrent under 50 kVp X-ray exposure with different doses is investigated in Fig. 6(b). The photocurrent of the device at −100 V reaches nearly 120 nA cm^{-2} when the dose rate is 71.73 μGy$_{air}$ s^{-1}, which indicates excellent X-ray detection performance for the PSC heterojunction photodiodes. Furthermore, the X-ray sensitivity (S) of the heterojunction photodiode could be calculated by the following equation:[49]

$$S = \frac{Q}{AX} \tag{5}$$

where Q is the photo charge collected during radiation, X is the radiation dose during the test, and A is the area of the region receiving radiation. As a result, S is approximately 1.72 × 10^3 μC Gy$_{air}$$^{-1}$ cm^{-2} for 50 kVp X-rays, as shown in Fig. 6(c). In order to compare the performance of previously reported X-ray detectors based on organic/inorganic lead bromide perovskite single crystals with this work, various relevant device parameters reported in the literature are summarized in Table 1. A comparison of the sensitivities obtained from published data reveals that the sensitivity of the PSC heterojunction X-ray detector is relatively high. This is attributed to the increased collected photo charges and decreased transit time of carriers due to the low dark current and high applied voltage bias. Moreover, the high mobility and low trap density of the PSC heterojunction benefit the transport of photogenerated carriers and reduce the recombination loss. The high sensitivity and response speed of the heterojunction detector at high bias exceed those of most state-of-the-art reported lead bromide perovskite detectors. It was also proved that the Bi^{3+}-doped MAPbCl$_3$ PSCs epitaxially grown on MAPbBr$_3$ PSCs to form a pN heterojunction help improve the response speed and enhance the X-ray detection performance.

Conclusion

In conclusion, we successfully fabricated a pN perovskite heterojunction device using a solution-processed epitaxy growth method. The as-fabricated MAPbBr$_3$/Bi^{3+}-doped MAPbCl$_3$ PSC heterojunction possesses a low trap density of about 4.59 × 10^9 cm^{-3} and carrier mobility of about 131 cm^2 V^{-1} s^{-1}. Compared to the Au–MAPbBr$_3$–Au device without built-in potential, the Au-PSC heterojunction-Au device shows smaller dark current, improved long term current stability and lower noise power density under the same conditions. The present PSC heterojunction photodiode shows a small dark current density and noise level under external reverse bias voltage due to the enlarged built-in potential of the pN heterojunction by Bi^{3+} doped in $MAPbCl_3$ PSCs. Additionally, the device indicates a relatively narrow bandwidth response in the visible range of the spectra, with a peak at 540 nm. Significantly, the as-fabricated $MAPbBr_3/Bi^{3+}$-doped $MAPbCl_3$ PSC heterojunction photodiode reveals excellent potential for application in direct X-ray detection, with a high sensitivity of up to 1.72×10^3 μC Gy_{air}^{-1} cm^{-2} for 50 kVp X-rays and a fast response time of up to 4.89 μs by applying an external 100 V reverse bias. The above results confirm that the fabrication of PSC heterojunctions by solution-processed epitaxial growth aids enhanced X-ray detection performance and may be a promising strategy to obtain superior perovskite single crystal X-ray detectors in future.

Author contributions

Y. P., X. W., Y. X. and J. Z. grew the perovskite single crystals. Y. P., conducted the epitaxial experiments. Y. P. and Y. L. conducted the measurements. X. W. and Y. P. analyzed the results. Y. P. wrote this manuscript. All the authors have made comments on the manuscript.

Conflicts of interest

The authors declare no competing financial interest.

Acknowledgements

The authors thank financial supports from the funding of National Key Research and Development Program of China (2018YFE0125500, 2016YFB0401600), Program 111_2.0 in China (BP0719013), National Natural Science Foundation Project of China (12005038, 61775034, 51879042, 61674029), Research Fund for International Young Scientists (62050410350), International cooperative research project of Jiangsu province (BZ2018056), Leading Technology of Jiangsu Basic Research Plan (BK20192003).

References

1 G. C. Xing, N. Mathews, S. Y. Sun, S. S. Lim, Y. M. Lam, M. Gratzel, S. Mhaisalkar and T. C. Sum, *Science*, 2013, **342**, 344–347.

2 Q. F. Dong, Y. J. Fang, Y. C. Shao, P. Mulligan, J. Qiu, L. Cao and J. S. Huang, *Science*, 2015, **347**, 967–970.

3 W. Mao, J. Zheng, Y. Zhang, A. S. R. Chesman, Q. Ou, J. Hicks, F. Li, Z. Wang, B. Graystone, T. D. M. Bell, M. U. Rothmann, N. W. Duffy, L. Spiccia, Y.-B. Cheng, Q. Bao and U. Bach, *Angew. Chem., Int. Ed.*, 2017, **56**, 12486–12491.

4 P. H. Wangyang, C. H. Gong, G. F. Rao, K. Hu, X. P. Wang, C. Y. Yan, L. P. Dai, C. Y. Wu and J. Xiong, *Adv. Opt. Mater.*, 2018, **6**, 1701302.

5 J. Miao and F. Zhang, *J. Mater. Chem. C*, 2019, **7**, 1741–1791.

6 S. D. Stranks and H. J. Snaith, *Nat. Nanotechnol.*, 2015, **10**, 391–402.

7 J. Q. Li, S. G. R. Bade, X. Shan and Z. B. Yu, *Adv. Mater.*, 2015, **27**, 5196–5202.

8 Q. Liao, X. Jin and H. B. Fu, *Adv. Opt. Mater.*, 2019, **7**, 1900099.

9 H. Y. Dong, C. H. Zhang, X. L. Liu, J. N. Yao and Y. S. Zhao, *Chem. Soc. Rev.*, 2020, **49**, 951–982.

10 M. A. Green, A. Ho-Baillie and H. J. Snaith, *Nat. Photonics*, 2014, **8**, 506–514.

11 N. J. Jeon, J. H. Noh, W. S. Yang, Y. C. Kim, S. Ryu, J. Seo and S. I. Seok, *Nature*, 2015, **517**, 476–480.

12 W. S. Yang, B. W. Park, E. H. Jung, N. J. Jeon, Y. C. Kim, D. U. Lee, S. S. Shin, J. Seo, E. K. Kim, J. H. Noh and S. I. Seok, *Science*, 2017, **356**, 1376–1379.

13 Y. C. Liu, Z. Yang, D. Cui, X. D. Ren, J. K. Sun, X. J. Liu, J. R. Zhang, Q. B. Wei, H. B. Fan, F. Y. Yu, X. Zhang, C. M. Zhao and S. Z. Liu, *Adv. Mater.*, 2015, **27**, 5176–5183.

14 D. Shi, V. Adinolfi, R. Comin, M. J. Yuan, E. Alarousu, A. Buin, Y. Chen, S. Hoogland, A. Rothenberger, K. Katsiev, Y. Losovyj, X. Zhang, P. A. Dowben, O. F. Mohammed, E. H. Sargent and O. M. Bakr, *Science*, 2015, **347**, 519–522.

15 M. I. Saidaminov, A. L. Abdelhady, B. Murali, E. Alarousu, V. M. Burlakov, W. Peng, I. Dursun, L. F. Wang, Y. He, G. Maculan, A. Goriely, T. Wu, O. F. Mohammed and O. M. Bakr, *Nat. Commun.*, 2015, **6**, 7586.

16 Y. N. Chen, M. H. He, J. J. Peng, Y. Sun and Z. Q. Liang, *Adv. Sci.*, 2016, **3**, 1500392.

17 G. Kakavelakis, M. Gedda, A. Panagiotopoulos, E. Kymakis, T. D. Anthopoulos and K. Petridis, *Adv. Sci.*, 2020, **7**, 2002098.

18 L. Basiricò, A. Ciavatti and B. Fraboni, *Adv. Mater. Technol.*, 2020, **6**, 2000475.

19 Y. Su, W. Ma and Y. Yang, *J. Semicond.*, 2020, **41**, 051204.

20 S. Kasap, *Nat. Photonics*, 2015, **9**, 420–421.

21 H. Wei, D. DeSantis, W. Wei, Y. Deng, D. Guo, T. J. Savenije, L. Cao and J. Huang, *Nat. Mater.*, 2017, **16**, 826–833.

22 Q. Xu, X. Wang, H. Zhang, W. Shao, J. Nie, Y. Guo, J. Wang and X. Ouyang, *ACS Appl. Electron. Mater.*, 2020, **2**, 879–884.

23 Q. Xu, W. Shao, Y. Li, X. Zhang, X. Ouyang, J. Liu, B. Liu, Z. Wu, X. Ouyang, X. Tang and W. Jia, *ACS Appl. Mater. Interfaces*, 2019, **11**, 9679–9684.

24 X. Wang, D. Zhao, Y. Qiu, Y. Huang, Y. Wu, G. Li, Q. Huang, Q. Khan, A. Nathan, W. Lei and J. Chen, *Phys. Status Solidi RRL*, 2018, **12**, 1800380.

25 S. Shrestha, R. Fischer, G. J. Matt, P. Feldner, T. Michel, A. Osvet, I. Levchuk, B. Merle, S. Golkar, H. Chen, S. F. Tedde, O. Schmidt, R. Hock, M. Rührig, M. Göken, W. Heiss, G. Anton and C. J. Brabec, *Nat. Photonics*, 2017, **11**, 436–440.

26 J. Song, X. Feng, H. Li, W. Li, T. Lu, C. Guo, H. Zhang, H. Wei and B. Yang, *J. Phys. Chem. Lett.*, 2020, **11**, 3529–3535.

27 Y. Pan, X. Wang, Y. Xu, Y. Li, E. E. Elemike, A. Shuja, Q. Li, X. Zhang, J. Chen, Z. Zhao and W. Lei, *Front. Chem.*, 2020, **8**, 791.

28 X. Wang, Y. Li, Y. Xu, Y. Pan, C. Zhu, D. Zhu, Y. Wu, G. Li, Q. Zhang, Q. Li, X. Zhang, J. Wu, J. Chen and W. Lei, *Chem. Mater.*, 2020, **32**, 4973–4983.

29 X. Wang, Y. Li, Y. Xu, Y. Pan, Y. Wu, G. Li, W. Zhang, S. Ding, J. Chen, W. Lei and D. Zhao, *Nano Mater. Sci.*, 2020, **2**, 292–296.

30 J. Euvrard, Y. Yan and D. B. Mitzi, *Nat. Rev. Mater.*, 2021, **6**, 531–549.

31 M. T. Klug, A. Osherov, A. A. Haghighirad, S. D. Stranks, P. R. Brown, S. Bai, J. T. W. Wang, X. Dang, V. Bulović, H. J. Snaith and A. M. Belcher, *Energy Environ. Sci.*, 2017, **10**, 236.

32 A. L. Abdelhady, M. I. Saidaminov, B. Murali, V. Adinolfi, O. Voznyy, K. Katsiev, E. Alarousu, R. Comin, I. Dursun, L. Sinatra, E. H. Sargent, O. F. Mohammed and O. M. Bakr, *J. Phys. Chem. Lett.*, 2016, **7**, 295–301.

33 C. Li, X. Chen, N. Li, J. Liu, B. Yuan, Y. Li, M. Wang, F. Xu, Y. Wu and B. Cao, *J. Mater. Chem. C*, 2020, **8**, 3694–3704.

34 L. Han, L. Wu, C. Liu and J. Zhang, *J. Phys. Chem. C*, 2019, **123**, 8578–8587.

35 M. A. Haque, J. L. Li, A. L. Abdelhady, M. I. Saidaminov, D. Baran, O. M. Bakr, S. H. Wei and T. Wu, *Adv. Opt. Mater.*, 2019, **7**, 1900865.

36 Z. Zhang, L. Ren, H. Yan, S. Guo, S. Wang, M. Wang and K. Jin, *J. Phys. Chem. C*, 2017, **121**, 17436–17441.

37 A. M. Ulatowski, A. D. Wright, B. Wenger, L. R. V. Buizza, S. G. Motti, H. J. Eggimann, K. J. Savill, J. Borchert, H. J. Snaith, M. B. Johnston and L. M. Herz, *J. Phys. Chem. Lett.*, 2020, **11**, 3681–3688.

38 R. Meng, G. Wu, J. Zhou, H. Zhou, H. Fang, M. A. Loi and Y. Zhang, *Chemistry*, 2019, **25**, 5480–5488.

39 Y. Yamada, M. Hoyano, R. Akashi, K. Oto and Y. Kanemitsu, *J. Phys. Chem. Lett.*, 2017, **8**, 5798–5803.

40 O. A. Lozhkina, A. A. Murashkina, V. V. Shilovskikh, Y. V. Kapitonov, V. K. Ryabchuk, A. V. Emeline and T. Miyasaka, *J. Phys. Chem. Lett.*, 2018, **9**, 5408–5411.

41 Y. Liu, Z. Yang, D. Cui, X. Ren, J. Sun, X. Liu, J. Zhang, Q. Wei, H. Fan, F. Yu, X. Zhang, C. Zhao and S. F. Liu, *Adv. Mater.*, 2015, **27**, 5176–5183.

42 G. Maculan, A. D. Sheikh, A. L. Abdelhady, M. I. Saidaminov, M. A. Haque, B. Murali, E. Alarousu, O. F. Mohammed, T. Wu and O. M. Bakr, *J. Phys. Chem. Lett.*, 2015, **6**, 3781–3786.

43 M. Bari, H. Wu, A. A. Bokov, R. F. Ali, H. N. Tailor, B. D. Gates and Z.-G. Ye, *CrystEngComm*, 2021, **23**, 3326–3339.

44 Y. X. Chen, Q. Q. Ge, Y. Shi, J. Liu, D. J. Xue, J. Y. Ma, J. Ding, H. J. Yan, J. S. Hu and L. J. Wan, *J. Am. Chem. Soc.*, 2016, **138**, 16196–16199.

45 W. Wang, H. Meng, H. Qi, H. Xu, W. Du, Y. Yang, Y. Yi, S. Jing, S. Xu, F. Hong, J. Qin, J. Huang, Z. Xu, Y. Zhu, R. Xu, J. Lai, F. Xu, L. Wang and J. Zhu, *Adv. Mater.*, 2020, **32**, 2001540.

46 Y. Chen, Y. Lei, Y. Li, Y. Yu, J. Cai, M. H. Chiu, R. Rao, Y. Gu, C. Wang, W. Choi, H. Hu, C. Wang, Y. Li, J. Song, J. Zhang, B. Qi, M. Lin, Z. Zhang, A. E. Islam, B. Maruyama, S. Dayeh, L. J. Li, K. Yang, Y. H. Lo and S. Xu, *Nature*, 2020, **577**, 209–215.

47 M. Tabatabaian, *COMSOL for Engineers*, Mercury Learning & Information, Dulles, VA, 2014.

48 Z. Cheng, K. Liu, J. Yang, X. Chen, X. Xie, B. Li, Z. Zhang, L. Liu, C. Shan and D. Shen, *ACS Appl. Mater. Interfaces*, 2019, **11**, 34144–34150.

49 M. Zahangir Kabir and S. O. Kasap, *J. Vac. Sci. Technol., A*, 2002, **20**, 1082–1086.

50 H. Zhang, F. Wang, Y. Lu, Q. Sun, Y. Xu, B.-B. Zhang, W. Jie and M. G. Kanatzidis, *J. Mater. Chem. C*, 2020, **8**, 1248–1256.

51 H. Wei, Y. Fang, P. Mulligan, W. Chuirazzi, H.-H. Fang, C. Wang, B. R. Ecker, Y. Gao, M. A. Loi, L. Cao and J. Huang, *Nat. Photonics*, 2016, **10**, 333–339.

52 L. Li, X. Liu, H. Zhang, B. Zhang, W. Jie, P. J. Sellin, C. Hu, G. Zeng and Y. Xu, *ACS Appl. Mater. Interfaces*, 2019, **11**, 7522–7528.